

# We are IntechOpen, the world's leading publisher of Open Access books Built by scientists, for scientists

**4,800**

Open access books available

**122,000**

International authors and editors

**135M**

Downloads

Our authors are among the

**154**

Countries delivered to

**TOP 1%**

most cited scientists

**12.2%**

Contributors from top 500 universities



**WEB OF SCIENCE™**

Selection of our books indexed in the Book Citation Index  
in Web of Science™ Core Collection (BKCI)

Interested in publishing with us?  
Contact [book.department@intechopen.com](mailto:book.department@intechopen.com)

Numbers displayed above are based on latest data collected.

For more information visit [www.intechopen.com](http://www.intechopen.com)



# Lithography-Free Nanostructure Fabrication Techniques Utilizing Thin-Film Edges

Hideo Kaiju<sup>1,2</sup>, Kenji Kondo<sup>1</sup> and Akira Ishibashi<sup>1</sup>

<sup>1</sup>Research Institute for Electronic Science, Hokkaido University

<sup>2</sup>PRESTO, Japan Science and Technology Agency  
Japan

## 1. Introduction

Fabricating nanoscale patterns with sub-10 nm feature size has been an important research target for potential applications in next-generation memories, microprocessors, logic circuits and other novel functional devices. Typically, according to the International Technology Roadmap for Semiconductor (ITRS) from 2009, an 8.9 nm node device is targeted for the year 2024. To achieve this milestone, liquid immersion lithography and extreme ultraviolet (EUV) lithography can be expected to be among the most commonly used techniques for the fabrication of nanopatterns. With liquid immersion lithography using a wavelength of 193 nm and a high numerical aperture (NA), it has been demonstrated that 32 nm features can be patterned (Finders et al., 2008; Sewell et al., 2009). EUV lithography using a short wavelength of 13.5 nm and 0.3-NA exposure tool has also enabled the printing of 22 nm half-pitch lines (Naulleau et al., 2009).

On the other hand, attractive patterning techniques, such as a superlattice nanowire pattern transfer (SNAP) method (Melosh et al., 2003; Green et al., 2007), a mold-to-mold cross imprint (MTMCI) process (Kwon et al., 2005) and a surface sol-gel process combined with photolithography (Fujikawa et al., 2006), are currently proposed and pursued actively. The SNAP method, which is based on translating thin film growth thickness control into planar wire arrays, has enabled the production of molecular memories consisting of 16 nm wide titanium/silicon nanowires. The MTMCI process using silicon nanowires formed by spacer lithography, in which nanoscale line features are defined by the residual part of a conformal film on the edges of a support structure with the linewidth controlled by the film thickness, has been used to produce a large array of 30 nm wide silicon nanopillars. With the surface sol-gel process combined with photolithography, where the linewidth is determined by the thickness of coating silica layer on the resist pattern, the size reduction and the large area of sub-20 nm silica walls have been achieved.

Recently, we have proposed a double nano-baumkuchen (DNB) structure, in which two thin slices of alternating metal/insulator nano-baumkuchen are attached so that the metal/insulator stripes cross each other, as part of a lithography-free nanostructure fabrication technology (Ishibashi, 2003 & 2004; Kaiju et al., 2008; Kondo et al., 2008). The schematic illustration of the fabrication procedure is shown in Fig. 1. First, the metal/insulator spiral heterostructure is fabricated using a vacuum evaporator including a film-rolled-up system. Then, two thin slices of the metal/insulator nano-baumkuchen

are cut out from the metal/insulator spiral heterostructure. Finally, the two thin slices are attached together face to face so that each stripe crosses in a highly clean environment (Ishibashi et al., 2005; Kaiju et al., 2005; Rahaman et al., 2008). Utilizing this DNB structure, we can expect to realize high density memory devices, the crossing point of which can be scaled down to ultimate feature sizes of a few nanometers thanks to their atomic-scale resolution of the film thickness determined by the rate of metal deposition, ranging from 0.01 to 1 nm/s. This DNB structure also gives a huge potential impact and importance of uniting bottom-up structures with top-down systems (Ishibashi, 2003). One element of the DNB structure is called a quantum cross (QC) device, which consists of two metal thin films (nanoribbons) having the edge-to-edge configuration as shown in Fig. 1 (Ishibashi, 2004; Kondo et al., 2006; Kaiju et al., 2008). In this QC device, the area of the crossed section is determined by the film thickness, in other words 1-20 nm thick films can produce  $1 \times 1$ - $20 \times 20$  nm<sup>2</sup> nanoscale junctions. Since the vacuum evaporation has good spatial resolution of one atomic layer thickness, the junction size of QC devices could ultimately be as small as a few ångströms square ( $10^{-2}$ nm<sup>2</sup>). This method offers a way to overcome the feature size limit of conventional optical lithography. When molecular-based self-assembled monolayers (SAMs), such as rotaxanes (Chen et al., 2003), catenanes (Balzani et al., 2000) and pseudorotaxanes (Pease et al., 2001), are sandwiched between the two thin metal films, QC devices can serve as novel non-volatile memory devices and switching devices. Moreover, when magnetic materials, such as Fe, Co and Ni, are used for the two thin metal films, QC devices can work as nanoscale spin injectors and tunneling magnetoresistance (TMR) devices. Among these devices, the resistance of the electrodes (thin metal films) can be reduced down to  $\sim$ k $\Omega$  since the width of films can be easily controlled to the one as long as  $\sim$ mm. This makes it possible to realize a highly sensitive detection for a junction resistance and to apply QC devices to high-frequency devices.

In this chapter, we present structural and electrical properties of Ni/polyethylene naphthalate (PEN) films used as electrodes in QC devices (Kaiju et al., 2009 & 2010) and current-voltage (*I-V*) characteristics for three types of QC devices. The three types of QC devices are as follows: (i) Ni/Ni QC devices (17 nm linewidth,  $17 \times 17$  nm<sup>2</sup> junction area), in which two Ni thin films are directly contacted with their edges crossed (Kondo et al., 2009; Kaiju et al., 2010), (ii) Ni/NiO/Ni QC devices (24 nm linewidth,  $24 \times 24$  nm<sup>2</sup> junction area), in which NiO thin insulators are sandwiched between two Ni thin-film edges (Kaiju et al., 2010) and (iii) Ni/poly-3-hexylthiophene (P3HT): 6, 6-phenyl C61-butyric acid methyl ester (PCBM)/Ni QC devices (16 nm linewidth,  $16 \times 16$  nm<sup>2</sup> junction area), in which P3HT:PCBM organic molecules are sandwiched between two Ni thin-film edges (Kaiju et al., 2010; Kondo et al., 2010). In our study, we have successfully fabricated various types of QC devices with nano-linewidth and nano-junctions, which have been obtained without the use of electron-beam or optical lithography. Our method will open up new opportunities for the creation of nanoscale patterns and can also be expected as novel technique beyond conventional lithography. Furthermore, we present the calculation results of the electronic transport in Ni/organic-molecule/Ni QC devices and discussed their possibility for switching devices. According to our calculation, a high switching ratio in excess of 100000:1 can be obtained under weak coupling condition. These results indicate that QC devices fabricated using thin-film edges can be expected to have potential application in next-generation switching devices with ultrahigh on-off ratios.

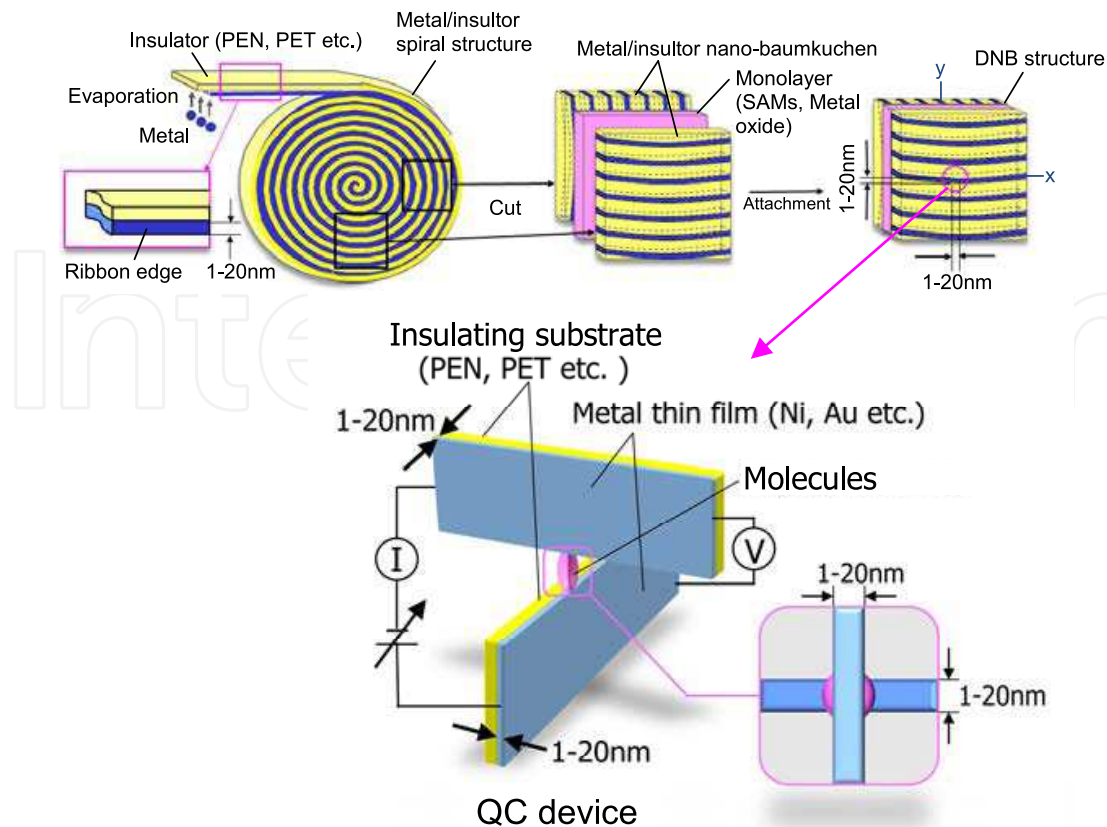


Fig. 1. Fabrication procedure of DNB structures and a schematic illustration of QC devices.

## 2. Fabrication and evaluation method of QC devices

### 2.1 Fabrication method of QC devices

The fabrication method of QC devices is shown in Fig. 2. First, Ni thin films were thermally evaporated on PEN organic substrates (2 mm width, 10 mm length and 25  $\mu\text{m}$  thickness) in a high vacuum chamber at a base pressure of  $\sim 10^{-8}$  torr. PEN organic substrates of TEONEX Q65 were supplied by Teijin DuPont Japan and cut down from 5 to 2 mm width using a slitter in a clean environment. A boron nitride crucible N-1, made by DENKA, and a tungsten filament, made by CRAFT, were used for the thermal evaporation of Ni thin films. A heat-block stainless plate with a hole was inserted between the Ni vapor source and the PEN substrate. The length of the crucible and the aperture size in the stainless plate were designed using a geometrical simulation to evaporate uniform Ni films in-plane to PEN substrates. The temperature near PEN substrates was less than 62  $^{\circ}\text{C}$ , which was lower than the glass transition temperature  $T_g$  of 120  $^{\circ}\text{C}$  for PEN substrates. The pressure during the evaporation was  $10^{-5}$  torr and the growth rate was 1.0-1.5 nm/min at an evaporation power of 280-350 W. Then, fabricated Ni/PEN films were sandwiched between two polymethyl methacrylate (PMMA) resins using epoxy. The volume of the PMMA resin was  $6 \times 3 \times 3 \text{ mm}^3$ . The edge of PMMA/Ni/PEN/PMMA structure was polished by chemical mechanical polishing (CMP) methods using alumina ( $\text{Al}_2\text{O}_3$ ) slurries with particle diameters of 0.1, 0.3 and 1.0  $\mu\text{m}$ . The polishing pressure was 6.5 psi and the platen rotation speed was 75 rpm. Finally, two sets of polished PMMA/Ni/PEN/PMMA structures were prepared and attached together with their edges crossed in a highly clean environment of ISO class minus 1. The attachment pressure

was 0.54 MPa and no glue was used. This is a basic process in fabricating QC devices. When Ni/Ni QC devices are fabricated, two Ni thin films are directly contacted with their edges crossed, as shown in Fig. 2(a). For the fabrication of Ni/NiO/Ni QC devices, after two sets of polished PMMA/Ni/PEN/PMMA structures were prepared, the Ni edge in one of the two samples was oxidized by O<sub>2</sub> plasma at a power of 5 W (= 5 mA and 1 kV) and then the oxidized and the unoxidized Ni edges were attached together with their edges crossed, as shown in Fig. 2(b). Also, for the fabrication of Ni/P3HT:PCBM/Ni QC devices, after two sets of polished PMMA/Ni/PEN/PMMA structures were prepared, P3HT:PCBM organic molecule blend was sandwiched between two sets of PMMA/Ni/PEN/PMMA structures whose edges were crossed, as shown in Fig. 2(c). P3HT and PCBM organic molecules were separately dissolved in monochlorobenzene, then blended together with a weight ratio of 1:1 to form a 20 mg/ml solution. This P3HT:PCBM solution was dripped on one of the polished PMMA/Ni/PEN/PMMA structure, then sandwiched by the other of the polished PMMA/Ni/PEN/PMMA structure. These three types of QC devices are shown in Fig. 2.

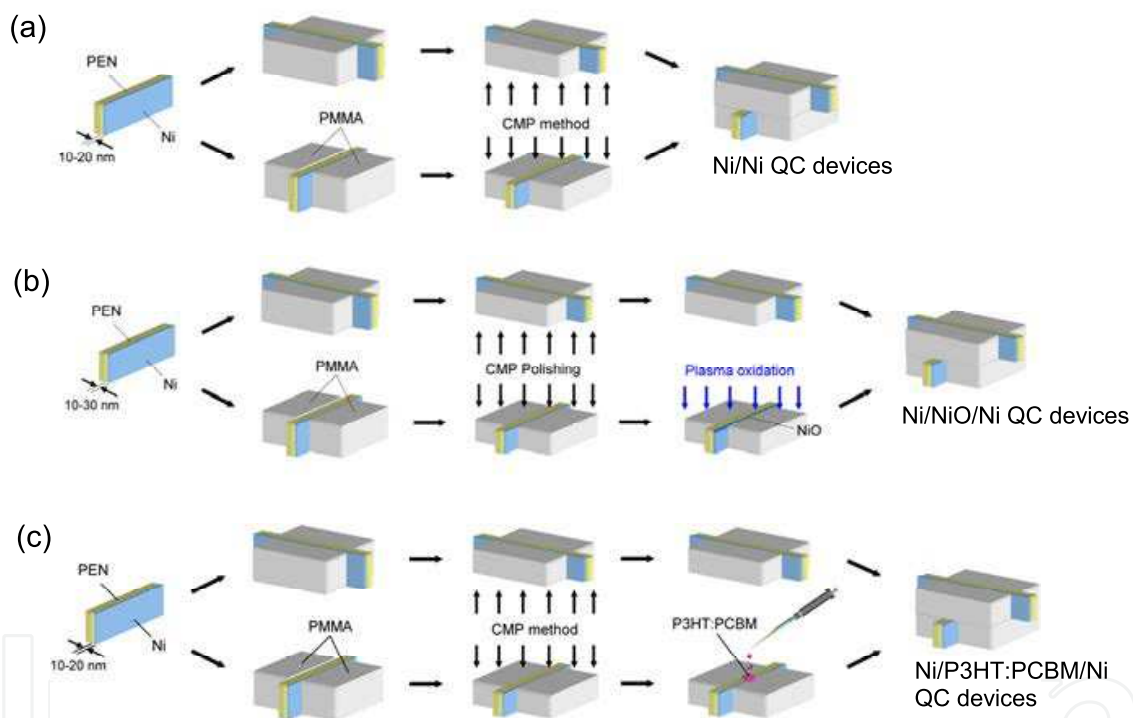


Fig. 2. Fabrication process of (a) Ni/Ni QC devices, (b) Ni/NiO/Ni QC devices and (c) Ni/P3HT:PCBM/Ni QC devices.

## 2.2 Evaluation methods of Ni/PEN films and QC devices

The Ni thickness was measured by a mechanical method using the stylus surface profiler DEKTAK and an optical method using the diode pumped solid state (DPSS) green laser at a wavelength of 532 nm and the photodiode detector. The surface morphologies of Ni/PEN samples were analyzed by atomic force microscope (AFM) Nanoscope IIIa. The microstructures as well as the Ni/PEN interfacial structures were examined using a JEOL JEM-3000F transmission electron microscope (TEM) operating at 300 kV. The cross-sectional TEM samples were prepared by a combination of mechanical polishing and Ar ion thinning. To reduce the beam-heating effects during ion thinning, the sample stage was cooled to -160

°C by liquid nitrogen conduction cooling. The  $I$ - $V$  characteristics of QC devices were measured by a four-probe method at room temperature.

### 3. Ni/PEN films used as electrodes in QC devices

#### 3.1 Cross-sectional TEM images of Ni/PEN films

Figs. 3(a) and (b) show the cross-sectional TEM images for Ni (20 nm)/PEN films. It can be seen that there is no diffusion of Ni into the PEN layer, resulting in clear and smooth formation of the Ni/PEN interface. Here, it should be noted that some researchers have reported that metal atoms diffuse into organic layers in the process of the metal evaporation onto organic layers (Tarlov, 1992; Hirose et al., 1996; Ito et al., 1999; Dürr et al., 2002). For example, the metastable atom electron spectroscopy (MAES) spectra of Au on the p-sexiphenyl (6P)/Au system shows that the features of 6P remain even though Au was deposited to about 20 nm thickness (Ito et al., 1999). This indicates that Au atoms or clusters penetrate into the 6P films. The soft x-ray photoemission spectroscopy (SXPS) investigation of the interface between evaporated indium and perylenetetracarboxylic dianhydride (PTCDA) also demonstrates that the interfacial region is very wide, ranging from 7 to 60 nm, and this means that the metal atoms of indium diffuse into PTCDA organic layers (Hirose et al., 1996). Moreover, according to studies on the interaction between evaporated Ag and octadecanethiol (ODT) on Au films using XPS, Ag deposited at 300 K migrates through the ODT layer and resides at the ODT/Au interface (Tarlov, 1992). As compared with above results, such a metal diffusion into organic layers does not occur in Ni/PEN interface. This indicates that Ni thin films on PEN organic substrates are suitable for metal/organic films used in QC devices. It can also be confirmed that the surface of Ni films is smooth, and this smoothness is in good agreement with the results of the AFM observation, where the surface roughness  $R_a$  is 1.1 nm. Fig. 3(c) shows the electron diffraction (ED) pattern for the same specimen. Ni thin films on PEN films have been shown to be face-centered-cubic structures, which are equal to those in bulk Ni structures. The ED pattern also shows that Ni thin films have polycrystalline structures, which can be recognized from the cross-sectional TEM image of Fig. 3(a). Thus, Ni /PEN films are suitable for QC devices from the viewpoint of the Ni/PEN interfacial and internal structures.

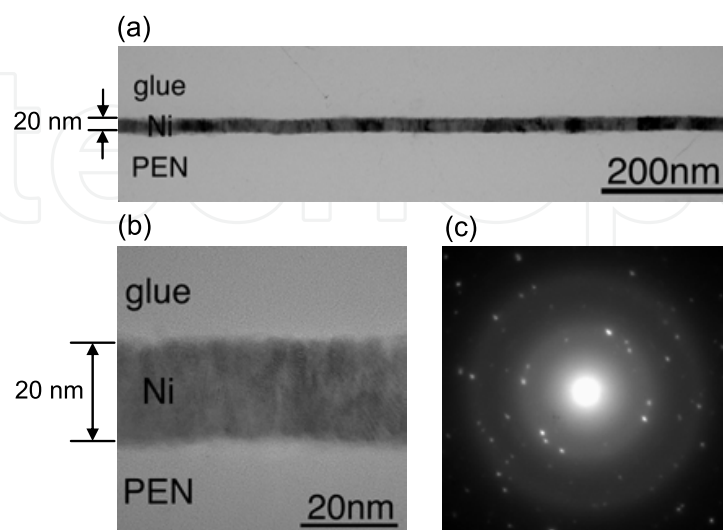


Fig. 3. (a) Cross-sectional TEM image, (b) high-resolution cross-sectional TEM image and (c) ED pattern for Ni (20 nm)/PEN films.

### 3.2 AFM surface morphology of Ni/PEN films

Fig. 4 shows the three-dimensional (3-D) surface images obtained from AFM observation for (a) PEN, (b) Ni (16 nm) /PEN and (c) Au (14 nm)/PEN. From the 3-D images, which are 500×500 nm<sup>2</sup> in area, mound-like surfaces are observed in Ni (16 nm)/PEN and Au (14 nm)/PEN, and are classified by the surface roughness  $R_a$ . Here, the surface roughness  $R_a$  is defined by

$$R_a = \frac{1}{L_x L_y} \int_0^{L_x} \int_0^{L_y} |h(x,y)| dx dy, \quad (1)$$

where  $h(x,y)$  is the height profile as a function of  $x$  and  $y$  and  $L_{x(y)}$  is the lateral scanning size in the  $x$  ( $y$ ) direction.  $R_a$  of PEN is 1.3 nm, which is smaller than that of widely-used organic films, such as polyethylene terephthalate (PET) and polyimide.  $R_a$  of Ni (16 nm)/PEN is also as small as 1.22 nm. In contrast,  $R_a$  of Au (14 nm)/PEN is as large as 2.53 nm. Fig. 5 shows the surface roughness as a function of the metal film thickness for Ni/PEN and Au/PEN.  $R_a$  increases up to 3.8 nm for a film thickness of 21 nm for Au/PEN. In comparison,  $R_a$  decreases slightly down to 1.1 nm with increasing the film thickness for Ni/PEN. Here, we consider the growth mode of Ni/PEN, and discuss their feasibility in QC devices from the viewpoint of the surface roughness. Fig. 6 shows the scaling properties of  $R_a$  for PEN and Ni/PEN. The inset represents the scaling properties of the root mean square (RMS) surface roughness  $R_q$ .  $R_q$  obeys a scaling law,  $R_q = w(L) \propto L^\alpha$ , where  $w(L)$  is the interface width corresponding to the standard deviation of the surface height,  $L$  is the system size and  $\alpha$  is the growth scaling exponent. The growth scaling exponent for roughening,  $w(L) \propto L^\alpha$ , has been widely used to characterize the growth of a solid from a vapor, such as the epitaxial growth of Fe/Si (111) (Chevrier et al., 1991), growth of evaporated Ag/quartz (Palasantzas et al., 1994) and molecular beam epitaxial growth of CuCl/CaF<sub>2</sub> (111) (Tong et al., 1994), as described by the Kardar-Parisi-Zhang (KPZ) equation (Kardar et al., 1986). As for PEN and Ni/PEN,  $\alpha$  shows the almost constant value of 0.67-0.68, as seen from the similar roughness slope in any sample. This indicates that the surface morphology of Ni/PEN exhibits almost the same behaviour as that of PEN and these results are consistent with the 3-D AFM observation in Fig. 4. We have also found that the surface is described as self-affine due to  $\alpha \neq \beta$ , where  $\beta$  is the dynamical exponent in a scaling law,  $R_q = w(L) \propto t_h^\beta$ . Here,  $t_h$  is a growth thickness. As one can see from Fig. 5,  $\beta$  is the negative value since the surface roughness slightly decreases with increasing the thickness for Ni/PEN. This results in  $\alpha \neq \beta$ , which shows the self-affine growth and it can also be seen in sputtered copper films (Ohkawa et al., 2002) and evaporated silver films on silicon substrates (Thompson et al., 2004). The growth process itself of Ni thin films on PEN organic substrates is of great interest and is rich in physics, so detailed work including the dynamic physical mechanism, such as the random deposition and ballistic deposition, will be reported elsewhere. Here, we consider their feasibility in QC devices from the viewpoint of the surface roughness. Since the junction area in QC devices is determined by the film thickness, we need to clarify the surface roughness in the same scanning scale as the thickness size. As shown in Fig. 6,  $R_a$ 's of Ni (16 nm)/PEN and PEN are 0.34 nm and 0.44 nm, respectively, which correspond to 2-3 atomic layers, in the scanning scale of 16 nm. This result suggests that the number of molecules sandwiched between two metal thin films in QC devices can be strictly determined in a high resolution of 2-3 atoms by controlling the thickness of Ni thin films and it leads to a high product yield of memory devices and switching devices due to the reduction of the fluctuation

in a junction resistance. These experimental results indicate that Ni/PEN films are suitable for QC devices from the viewpoint of the surface, interface and internal structures.

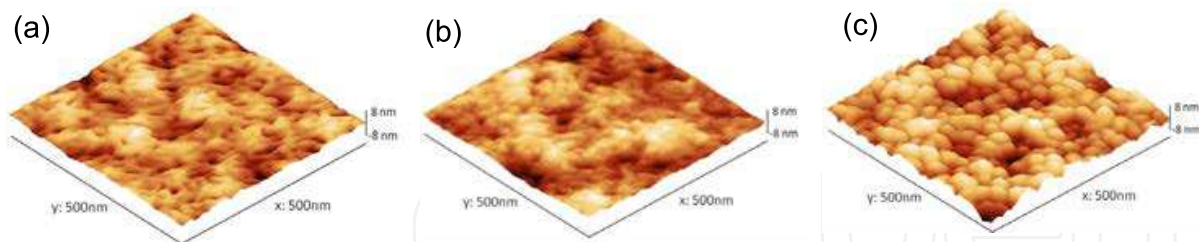


Fig. 4. 3-D surface images obtained from AFM observation for (a) PEN, (b) Ni (16 nm)/PEN and (c) Au (14 nm)/PEN.

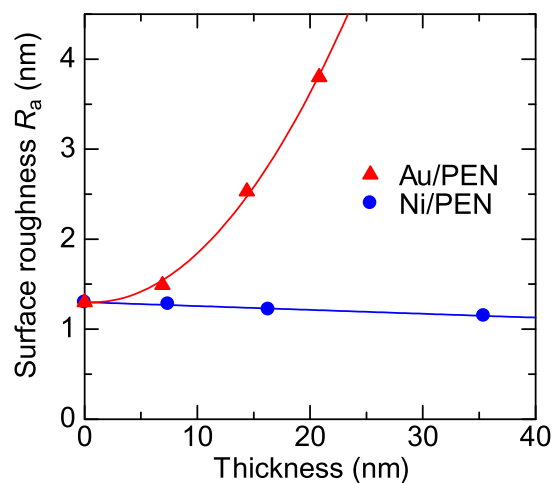


Fig. 5. Surface roughness as a function of the metal film thickness for Ni/PEN and Au/PEN.

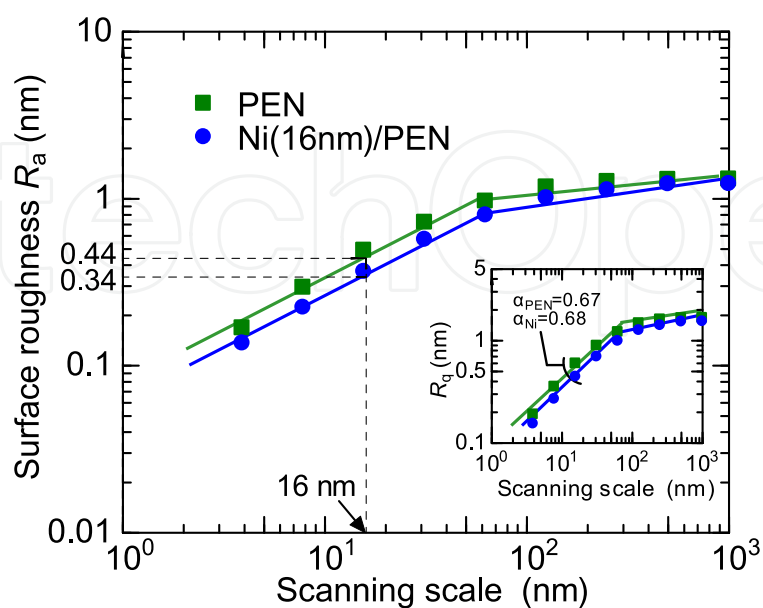


Fig. 6. Scaling properties of the surface roughness  $R_a$  for PEN and Ni/PEN. The inset represents the scaling properties of the RMS surface roughness  $R_q$ .



### 3.3 Electric resistivity of Ni/PEN films

Fig. 7 shows the Ni thickness dependence of the electric resistivity for Ni thin films on PEN substrates. The electric resistivity  $\rho_{\text{Ni}}$  increases with decreasing the Ni thickness  $d$ . In order to explain this experimental result quantitatively, we have calculated the electric resistivity using Mayadas-Shatzkes model (Mayadas et al., 1970). According to Mayadas-Shatzkes model, the electric resistivity  $\rho_{\text{Ni}}$  is expressed by

$$\rho_{\text{Ni}} / \rho_0 = \left[ 1 - \frac{3}{2}\alpha + 3\alpha^2 - 3\alpha^3 \ln\left(1 + \frac{1}{\alpha}\right) \right]^{-1}, \quad (2)$$

$$\alpha = \frac{\lambda}{D} \frac{R_g}{1 - R_g}, \quad (3)$$

where  $\lambda$  is the electron mean free path,  $D$  is the average grain diameter,  $R_g$  is the reflection coefficient for electrons striking the grain boundary and  $\rho_0$  is the electric resistivity for bulk Ni. The electron mean free path  $\lambda$  is 11 nm for bulk Ni. The average grain diameter  $D$  is 3 nm, which has been obtained from the high-resolution TEM image and the ED pattern. The reflection coefficient  $R_g$  is 0.71-0.95, which is the extrapolation value obtained from  $R_g$  in Ni thin films with the thickness of 31-115 nm (Nacereddine et al., 2007). From Fig. 7, the experimental result shows good agreement with the calculation result quantitatively. This means that the main contribution to the electric resistivity comes from the electron scattering at grain boundaries in Ni thin films on PEN substrates. Here, we discuss the use of Ni thin films on PEN substrates for electrodes of QC devices. As can be seen from Fig. 7, the electric resistivity of Ni thin films on PEN substrates is 1-2 orders larger than that of bulk Ni. This large resistivity could produce high-resistance electrodes in QC devices. However, as stated in the introduction of this chapter, the electrode resistance can be reduced down since the film width can be controlled to the one as long as  $\sim$ mm. Fig. 8(a) shows the Ni electrode resistance as a function of the linewidth  $l$ , which corresponds to the Ni thickness  $d$ , in QC devices. The schematic illustration of QC devices is shown in Fig. 8(b). In Fig. 8(a), Ni electrode resistances in the conventional cross-bar structures are also shown. The black solid line, dashed line and dotted line represent Ni electrode resistances estimated in conventional cross-bar structures with aspect ratios of 1:1, 3:1 and 5:1, respectively, where the resistivity is assumed to be the reported value in Ni thin films on glass substrates (Vries, 1987). The schematic illustration of conventional cross-bar structures is shown in Fig. 8(c). From Fig. 8(a), Ni electrode resistances in the conventional cross-bar structures are larger than 0.74, 1.2 and 3.7 M $\Omega$  in aspect ratios of 5:1, 3:1 and 1:1, respectively, for a linewidth of less than 20 nm. In contrast, QC devices show electrode resistances as small as 0.3-2 k $\Omega$  for a linewidth of 10-20 nm. This resistance reduction in Ni electrodes makes it possible to detect the resistance of sandwiched materials between two edges of Ni thin films very strictly and precisely and also this result indicates that QC devices have potential application in high-frequency devices. Thus, Ni/PEN films are suited for electrodes in QC devices from the viewpoint of the electrical properties as well as the surface, interface and internal structures.

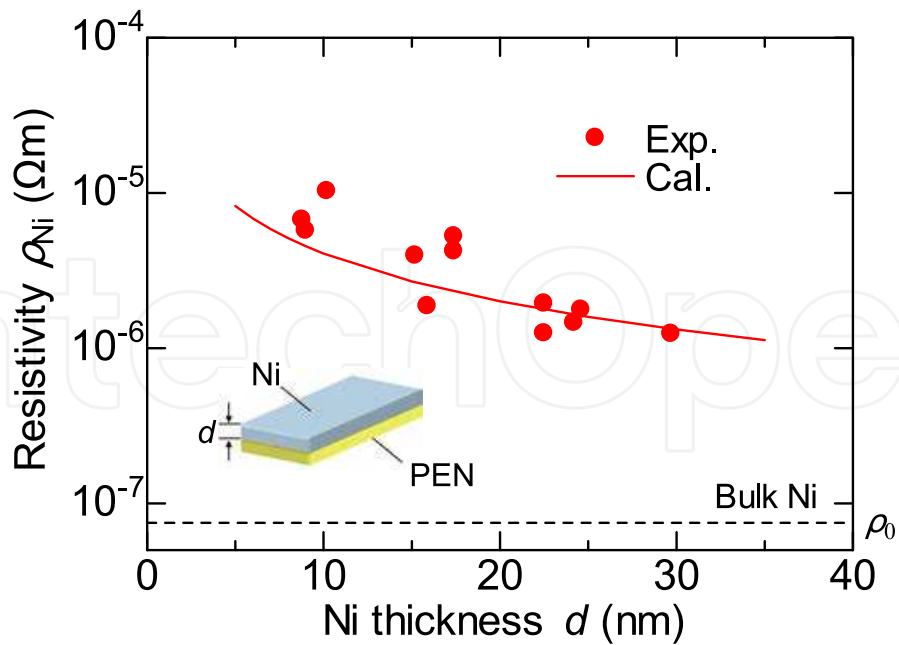


Fig. 7. Ni thickness dependence of the electric resistivity for Ni thin films on PEN substrates.

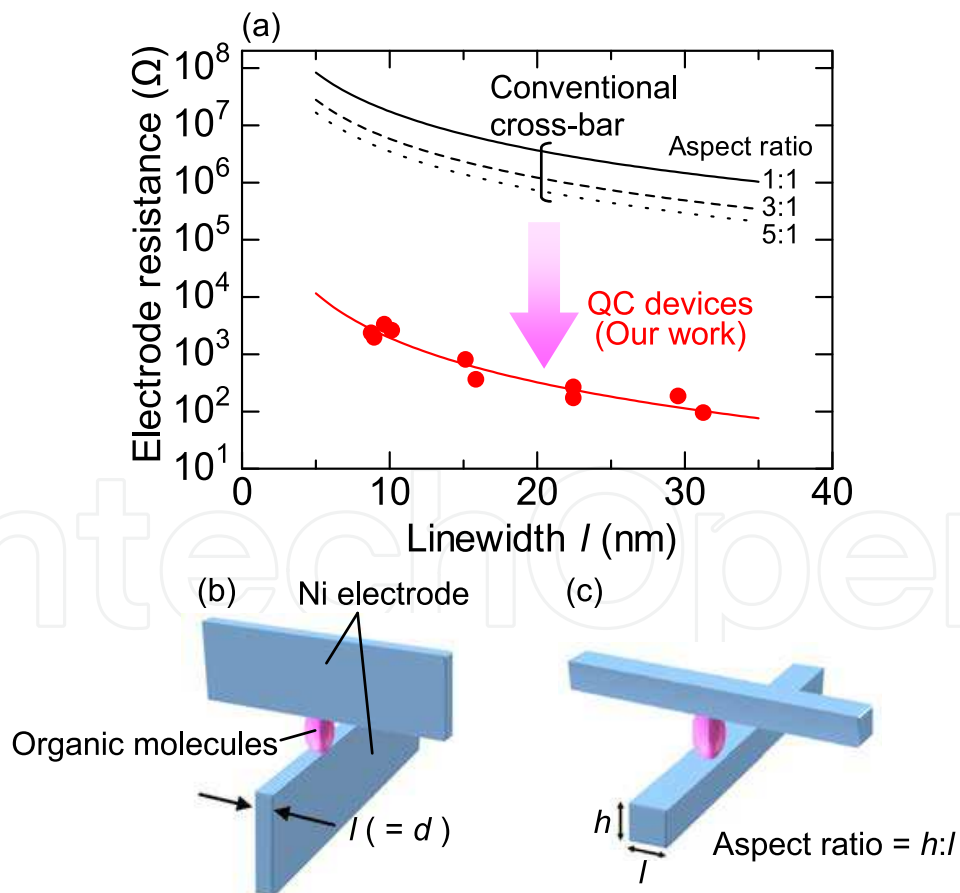


Fig. 8. (a) Ni electrode resistance as a function of the linewidth  $l$ , which corresponds to the Ni thickness  $d$ , in QC devices. Schematic illustration of (b) QC devices and (c) conventional cross-bar structures.

#### 4. Electrical properties of QC devices

##### 4.1 I-V characteristics of Ni/Ni QC devices

Fig. 9 shows the  $I$ - $V$  characteristics for Ni/Ni QC devices fabricated using Ni/PEN films discussed above. The inset shows the experimental setup for the four-probe method. Since the Ni thickness is 17 nm, the cross-sectional area between two Ni thin films is  $17 \times 17 \text{ nm}^2$ . As seen from Fig. 9, the ohmic  $I$ - $V$  characteristics have been obtained for both positive and negative bias at room temperature. Fig. 10 shows the aging properties for the voltage with constant currents of 0.1, 0.2, 0.3, 0.5, 0.7 and  $1.0 \mu\text{A}$ , respectively. The voltage is stable in any current and the standard deviation  $\Delta V$  of the voltage is 22-25 mV, which corresponds to the signal-to-noise (SN) ratio of 34-52 dB, where the SN ratio is defined by  $20 \log V/\Delta V$ . Here, it should be noted that the fabrication of nanojunctions using the film edges had been challenged by other researchers before (Nawate, et al., 2004). According to their attempts, Co and Ni thin films were evaporated onto glass substrates using vacuum evaporation and then they were cleaved and stuck to each other with their edges crossing. Although the current flowed across the junction, there remained a few problems: that the edge angle had to be inclined at a  $15$ - $25^\circ$  and the film thickness had to be larger than 50 nm. Furthermore, the current was slightly changed as time passed although the current flowed. In contrast, such problems have not occurred in our experiments, and we have obtained stable ohmic characteristics, where there has been no change with time, for the 17 nm size junction. These experimental results indicate that our method using thin-film edges can be expected to work as a new nanostructure fabrication technology beyond conventional lithography.

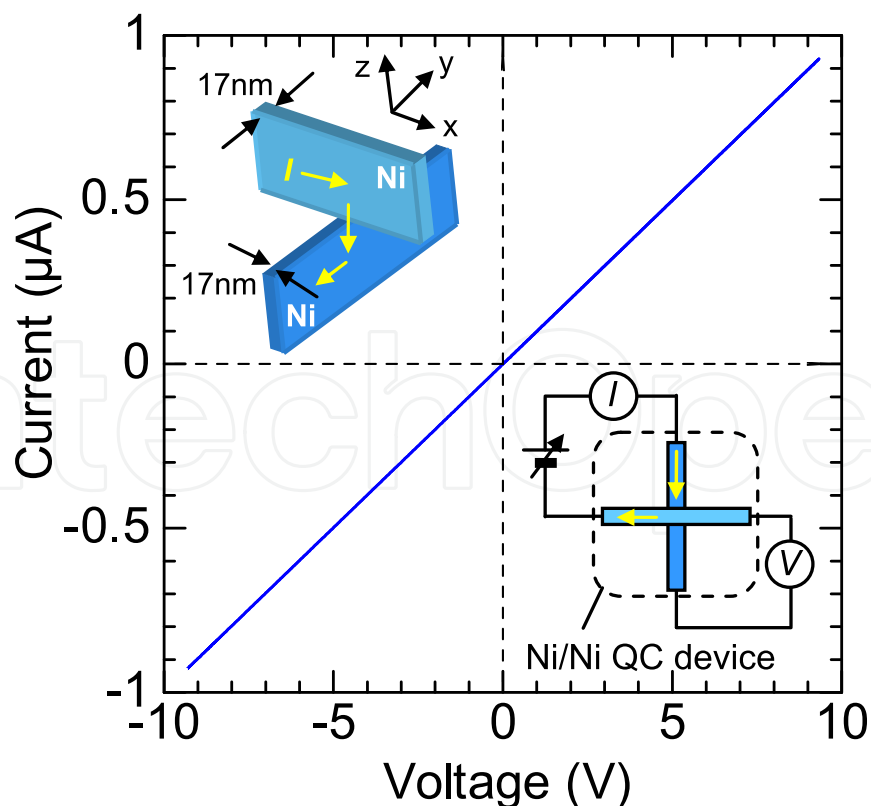


Fig. 9.  $I$ - $V$  characteristics for Ni/Ni QC devices with a junction area of  $17 \times 17 \text{ nm}^2$ . The inset shows the experimental setup for the four-probe method.

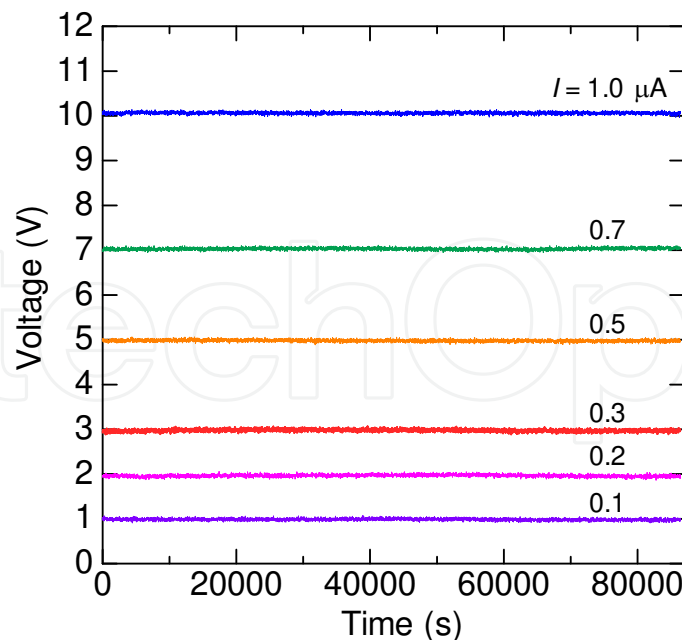


Fig. 10. Aging properties for Ni/Ni QC devices with a junction area of  $17 \times 17 \text{ nm}^2$ .

#### 4.2 J-V characteristics of Ni/NiO/Ni QC devices

In this section, we present current density-voltage ( $J$ - $V$ ) characteristics in Ni/NiO/Ni QC devices, which consist of NiO tunnel barriers sandwiched between two Ni thin films whose edges are crossed. First, we introduce the background of sub-micrometer scale tunnel junctions and the motivation for fabricating QC devices with tunnel barriers. Then, we show the derivation of a formula for  $J$ - $V$  characteristics of QC devices with tunnel barriers and finally demonstrate experimental results of their  $J$ - $V$  characteristics.

##### 4.2.1 Background of sub-micrometer scale tunnel junctions

Sub-micrometer scale tunnel junctions have attracted much interest due to their potential application in magnetic random access memories (MRAMs), fast detectors of terahertz (THz) and IR radiation and superconducting quantum interference devices (SQUIDs). Magnetic tunnel junctions (MTJs), which consist of two ferromagnetic metals separated by thin insulators, can be expected as ultrahigh-density MRAM devices because of the giant TMR effect at room temperature (Miyazaki et al., 1995; Moodera et al., 1995; Yuasa et al., 2004; Parkin et al., 2004). CoFeB/MgO/CoFeB MTJs with a small junction area of  $0.02 \text{ } \mu\text{m}^2$  exhibit a large TMR ratio of 98 %, where a clear current-induced magnetization switching (CIMS) with a low switching current density of  $3.6 \text{ MA/cm}^2$  have been observed (Hayakawa et al., 2008). Antenna-coupled tunnel junction devices, which consist of metal/insulator/metal tunnel junctions coupled to a thin-film metal antenna, can also be expected as fast detectors of THz and IR radiation (Sanchez et al., 1978; Kale, 1985; Hobbs et al., 2005). Ni/NiO/Ni tunnel junctions with a junction area of  $0.16 \text{ } \mu\text{m}^2$  coupled to thin-film metal antennas can serve as IR detectors and frequency mixers in the  $10 \text{ } \mu\text{m}$  band (Wilke et al., 1994; Fumeaux et al., 1996). Moreover, much effort has been devoted to the development of sub-micrometer scale SQUIDs, which are very promising devices with a high magnetic flux sensitivity (Rugar et al., 2004; Troeman et al., 2007; Huber et al., 2008; Kirtley et al., 2009). Aluminum SQUIDs with an effective area of  $0.034 \text{ } \mu\text{m}^2$  display a high flux sensitivity

of  $1.8 \times 10^{-6} \Phi_0/\text{Hz}^{1/2}$ , where  $\Phi_0 = h/2e$  is the flux quantum, and operates in fields as high as 0.6 T (Finkler et al., 2010). Thus, sub-micrometer scale tunnel junctions can find a wide range application in various functional electronic devices.

As shown in the previous section, our nanostructure fabrication method using thin-film edges offers a way to overcome the feature size limit of conventional lithography. This method can be extended to fabricating nanoscale tunnel junctions. The realization of nanoscale tunnel junctions leads to the enhancement of the performance in MRAMs, fast detectors of THz and IR radiation and SQUIDs. From this motivation, it is of great importance to fabricate QC devices with tunnel barriers and very meaningful to investigate their  $J$ - $V$  characteristics.

#### 4.2.2 Derivation of a formula for $J$ - $V$ characteristics of QC devices with tunnel barriers

We derive a formula for  $J$ - $V$  characteristics in QC devices with tunnel barriers, which consist of thin insulating barriers sandwiched between two thin metal films whose edges are crossed, shown in Fig. 11. The thicknesses of the top and bottom metal films are  $l_z$  and  $l_y$ , respectively. The barrier height and the barrier thickness are  $\phi$  and  $d$ , respectively. The number of electrons per unit area and unit time from the top to bottom metal is given by

$$\begin{aligned} N_S^T &= \int_0^\infty v_x n(v_x) |T(v_x)|^2 dv_x \\ &= \frac{1}{2\pi} \int_0^\infty \frac{1}{\hbar} \frac{\partial E}{\partial k_x} n(k_x) |T(k_x)|^2 dk_x, \end{aligned} \quad (4)$$

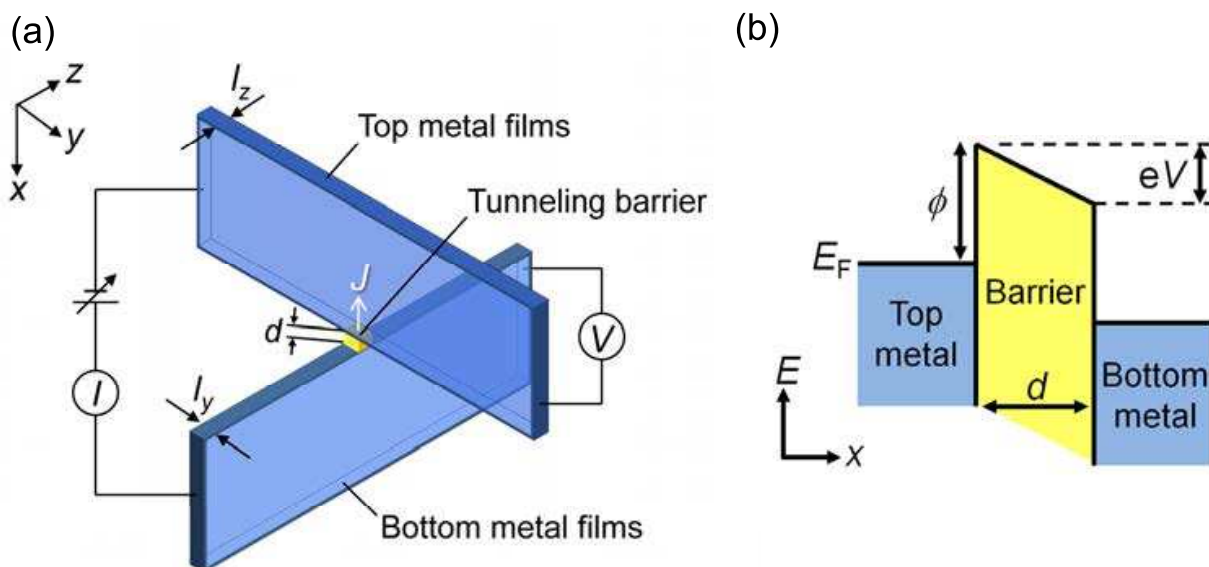


Fig. 11. (a) QC devices with tunnel barriers and (b) the potential profile of the barrier, which is used for the calculation of the transmission probability.

where  $v_x$  is the  $x$ -direction velocity,  $n(v_x)$  is the number of electrons per unit volume and unit velocity,  $k_x$  is the  $x$ -direction wave number,  $n(k_x)$  is the electron density,  $\hbar$  is Planck's constant divided by  $2\pi$  and  $E$  is the total energy of electrons, which is expressed by

$$\begin{aligned}
 E &= E_x + E_y + E_z \\
 &= \frac{\hbar^2}{2m} \left\{ k_x^2 + k_y^2 + \left( \frac{n\pi}{l_z} \right)^2 \right\},
 \end{aligned} \tag{5}$$

where  $E_x$ ,  $E_y$  and  $E_z$  are the  $x$ ,  $y$  and  $z$  components of the total energy of electrons, respectively,  $m$  is the electron mass,  $k_y$  is the  $y$ -direction wave number and  $n$  is the positive integer.  $T(k_x)$  is the transmission probability of electrons through the barrier.  $T(k_x)$  is calculated by the well-known Wentzel-Kramers-Brillouin (WKB) approximation. The potential profile is illustrated in Fig. 11(b). Here, the electron density is given by

$$n(k_x) = \frac{1}{2\pi^2} \int_0^\infty \int_0^\infty f(E) dk_y dk_z, \tag{6}$$

where  $f(E)$  is the Fermi-Dirac distribution function. Substituting Eqs. (5) and (6) in Eq. (4) yields

$$N_S^T = \frac{1}{4\pi^3 \hbar} \int_0^\infty |T(k_x)|^2 \left[ \int_0^\infty \int_0^\infty f(E) dk_y dk_z \right] dE_x. \tag{7}$$

Since the density of states in the  $k_y$  direction for the top metal is equal to the solution of one-dimensional density of states, the relation between  $k_y$  and  $E_y$  is given by

$$dk_y = \frac{m}{\hbar \sqrt{2mE_y}} dE_y. \tag{8}$$

Substituting Eqs. (5) and (8) in Eq. (7) gives

$$N_S^T = \frac{1}{4\pi^3 \hbar} \int_0^\infty |T(k_x)|^2 \left[ \sum_{n=1}^\infty \int_0^\infty f(E) \frac{m}{\hbar \sqrt{2mE_y}} \theta \left( E_y - \frac{\hbar^2}{2m} \left( \frac{n\pi}{l_z} \right)^2 \right) dE_y \right] dE_x, \tag{9}$$

where  $\theta(x)$  is the unit step function. The number of electrons per unit area and unit time from the bottom to top metal is also derived in a similar manner. When the positive bias  $V$  is applied to the bottom metal, the Fermi-Dirac distribution function is written by  $f(E+eV)$ . Thus, the number of electrons from the bottom to top metal is

$$N_S^B = \frac{1}{4\pi^3 \hbar} \int_0^\infty |T(k_x)|^2 \left[ \sum_{n=1}^\infty \int_0^\infty f(E+eV) \frac{m}{\hbar \sqrt{2mE_z}} \theta \left( E_z - \frac{\hbar^2}{2m} \left( \frac{n\pi}{l_y} \right)^2 \right) dE_z \right] dE_x. \tag{10}$$

Consequently, we obtain for the net current density  $J$  through the barrier

$$\begin{aligned}
 J &= e(N_S^T - N_S^B) \\
 &= \frac{e}{4\pi^3 \hbar} \int_0^\infty |T(k_x)|^2 \left[ \sum_{n=1}^\infty \int_0^\infty f(E) \frac{m}{\hbar \sqrt{2mE_y}} \theta \left( E_y - \frac{\hbar^2}{2m} \left( \frac{n\pi}{l_z} \right)^2 \right) dE_y \right. \\
 &\quad \left. - \sum_{n=1}^\infty \int_0^\infty f(E+eV) \frac{m}{\hbar \sqrt{2mE_z}} \theta \left( E_z - \frac{\hbar^2}{2m} \left( \frac{n\pi}{l_y} \right)^2 \right) dE_z \right] dE_x.
 \end{aligned} \tag{11}$$

We can calculate  $J$ - $V$  characteristics as a function of the metal thickness, the barrier height and the barrier thickness using Eq. (11).

#### 4.2.3 J-V characteristics of Ni/NiO/Ni QC devices

Fig. 12 shows the  $J$ - $V$  characteristics for Ni/NiO/Ni QC devices at room temperature. Since the Ni thickness is 24 nm, the junction area is  $24 \times 24 \text{ nm}^2$ . In Fig. 12(a), solid circles are experimental data and dashed, solid and dotted lines are calculation results for barrier heights of 0.6, 0.8 and 1.0 eV, respectively, with a constant barrier thickness of 0.63 nm. In Fig. 12(b), solid circles are experimental data and dashed, solid and dotted lines are calculation results for barrier thicknesses of 0.42, 0.63 and 0.84 nm, respectively, with a barrier height of 0.8 eV. As seen from Fig. 12, experimental results are in good agreement with calculation results for a barrier height of 0.8 eV and a barrier thickness of 0.63 nm. Since the crystal structure of NiO is a NaCl-type structure with a lattice constant  $a = 0.42 \text{ nm}$ , 2 monolayer of NiO is formed as shown in the inset of Fig. 12. Here, we discuss the barrier height of NiO insulating layers. The bulk NiO is a charge-transfer insulator, which has been approved by X-ray absorption (Kuiper et al., 1989) and X-ray photoemission and bremsstrahlung isochromat spectroscopy (Sawatzky et al., 1984; Elp et al., 1992). According

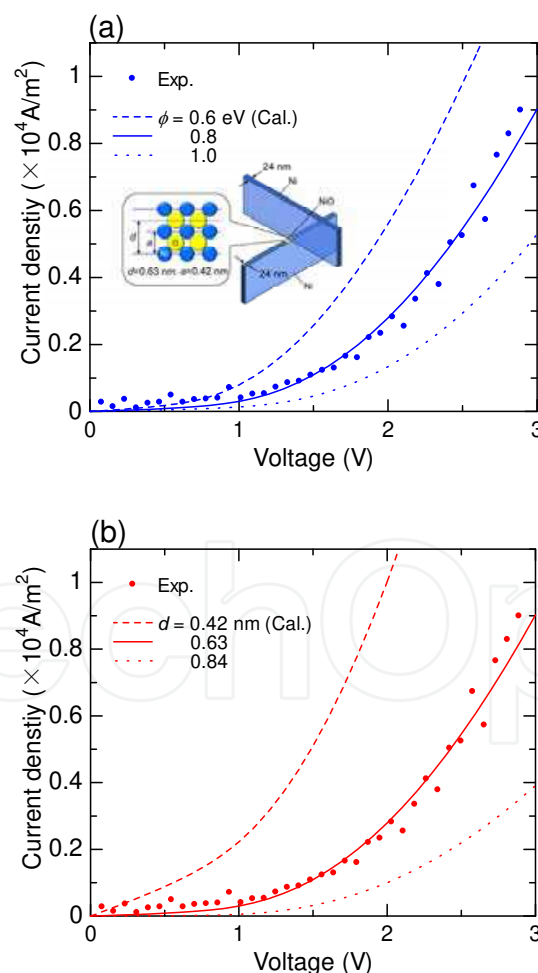


Fig. 12. (a) Barrier height dependence and (b) barrier thickness dependence of  $J$ - $V$  characteristics for Ni/NiO/Ni QC devices with a junction area of  $24 \times 24 \text{ nm}^2$  at room temperature.

to these experiments, the energy gap is 4.0-4.3 eV, which agrees with recent calculation results performed using the full-potential linearized augmented plane wave (FLAPW) method within the LSDA(GGA)+U (LSDA, local-spin-density approximation; GGA, generalized gradient approximation; U, on-site Coulomb interaction) (Cai et al., 2009). Since the Fermi energy of NiO is located in the level of 1.0 eV higher than the top of the valence band (Sawatzky et al., 1984), the barrier height in metal/NiO/metal tunnel junctions is estimated to be 3.0-3.3 eV. However, several researchers have reported that the barrier height in metal/NiO/metal tunnel junctions tends to become smaller than the estimated value of 3.0-3.3 eV (Doudin et al., 1997; Ono et al., 1997; Hobbs et al., 2005). For example, the barrier height of Ni/NiO/Ni tunnel junctions with a junction area of  $0.3 \mu\text{m}^2$  is as low as 0.18-0.22 eV with a barrier thickness of 2.5 nm (Hobbs et al., 2005). Electrodeposited Ni/NiO/Co tunnel junctions with a cross section of  $0.01 \mu\text{m}^2$  exhibit a low barrier height of 0.2-0.4 eV with a barrier thickness of 2-3 nm (Doudin et al., 1997). Thus, the barrier height of NiO thin films is reported to be smaller than that of NiO bulk materials. In our experiments, the barrier height in Ni/NiO/Ni QC devices is also estimated to be as low as 0.8 eV. This means that the derived formula is useful for the evaluation of the barrier height and the barrier thickness in QC devices with tunnel barriers. This fact also indicates that high-quality NiO thin films were formed and Ni/NiO/Ni QC devices worked well as nanoscale tunnel devices. Therefore, our method to fabricate nanoscale junctions utilizing thin-film edges can be expected to work as a new technique for the creation of nanoscale tunnel junctions.

#### 4.3 I-V characteristics of Ni/P3HT:PCBM/Ni QC devices

In this section, we present *I-V* characteristics in Ni/P3HT:PCBM/Ni QC devices, which consist of P3HT:PCBM organic molecules sandwiched between two Ni thin films whose edges are crossed. First, we introduce the background of molecular electronic devices and the motivation for fabricating QC devices with organic molecules. Then, we show the theoretical calculation for *I-V* characteristics of QC devices with organic molecules and compare them with experimental results. Finally, we discuss their possibility for switching devices with high on-off ratios.

##### 4.3.1 Background of molecular electronic devices

Molecular electronics have stimulated considerable interest as a technology that offers the prospect of scaling down device dimensions to a few nanometers and that also promotes a practical introduction to high-density memory applications (Chen et al., 1999; Reed et al., 2001; Chen et al., 2003; Lau et al., 2004; Wu et al., 2005; Mendes et al., 2005; Green et al., 2007). Especially, in the ITRS 2009 edition, molecular memory devices have been expected as candidates for beyond-CMOS devices since they offer the possibility of nanometer-scale components. For examples, Au/2'-amino-4-ethynylphenyl-4'-ethynylphenyl-5'-nitro-1-benzenethiolate/Au molecular devices with a junction area of  $30 \times 30$ - $50 \times 50 \text{ nm}^2$  have been fabricated using nanopore methods, and have exhibited a negative differential resistance and a large on-off peak-to-valley ratio (Chen et al., 1999). Molecular devices, which comprise a monolayer of bistable [2]rotaxanes sandwiched between two Ti/Pt metal electrodes with a linewidth of 40 nm, have also been fabricated using nanoimprint lithography, and have shown bistable *I-V* characteristics with high on-off ratios and reversible switching properties (Chen et al., 2003). Moreover, cross-bar molecular devices



consisting of a monolayer of bistable [2]rotaxanes sandwiched between top Ti and bottom Si electrodes (16 nm wide at 33 nm pitch) have been fabricated using SNAP methods, and have acted as 160 kbit memories patterned at a density of 100 Gbit/cm<sup>2</sup> (Green et al., 2007). Thus, molecular electronic devices can be expected as next-generation high-density memories.

As demonstrated in the previous section, our method using thin-film edges provides the fabrication of nanoscale tunnel junctions. This method can be extended to fabricating nanoscale molecular devices. The realization of nanoscale molecular devices leads to the application in next-generation high-density memories. From this motivation, it is of great significance to fabricate QC devices with organic molecules and very interesting to investigate their  $I$ - $V$  characteristics.

#### 4.3.2 Theoretical calculation and experimental results of $I$ - $V$ characteristics in Ni/P3HT: PCBM/Ni QC devices

We calculate the  $I$ - $V$  characteristics of QC devices with the molecule within the framework of Anderson model (Kondo et al., 2008 & 2009; Kondo, 2010). QC devices with the molecule consist of the molecule sandwiched between two thin metal films whose edges are crossed. The molecule is assumed to have two energy levels. In this calculation model, the Anderson Hamiltonian is given by

$$H = H_{\text{electrodes}} + H_{\text{molecules}} + H_{\text{t}}. \quad (12)$$

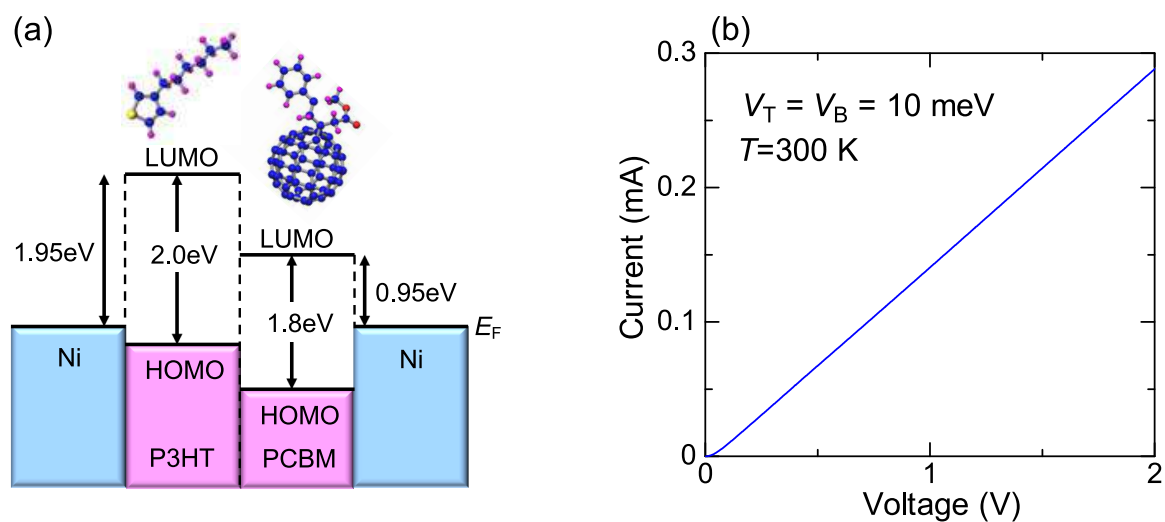


Fig. 13. (a) Energy diagram used in the calculation of  $I$ - $V$  characteristics for QC devices and (b) the calculated  $I$ - $V$  characteristics for QC devices under the strong coupling limit.

Here,  $H_{\text{electrodes}}$  is the Hamiltonian of both of the metal electrodes,  $H_{\text{molecules}}$  is the Hamiltonian of the molecule sandwiched between the metal electrodes and  $H_t$  is the transfer Hamiltonian between the sandwiched molecule and each electrode.  $H_{\text{electrodes}}$ ,  $H_{\text{molecules}}$  and  $H_t$  can be expressed by

$$\begin{aligned} H_{\text{electrodes}} &= \sum_{\alpha=T,B} \sum_{k,\sigma} \varepsilon_{k\sigma} c_{\alpha,k\sigma}^+ c_{\alpha,k\sigma}, \\ H_{\text{molecules}} &= \sum_{i,\sigma} \varepsilon_0(i) a_{i,\sigma}^+ a_{i,\sigma}, \\ H_t &= \sum_{\alpha=T,B} \sum_{k,\sigma} \sum_{i,\sigma} (V_{\alpha} c_{\alpha,k\sigma}^+ a_{i,\sigma} + h.c.). \end{aligned} \quad (13)$$

Here,  $\varepsilon_{k\sigma}$  is the free electron energy of  $\hbar^2 k^2 / 2m$ , where  $m$  is the free electron mass,  $\hbar$  is Planck's constant divided by  $2\pi$  and  $k$  is a two-dimensional wavenumber.  $c_{\alpha,k\sigma}^+$  and  $c_{\alpha,k\sigma}$  are creation and annihilation operators for electrons of wavenumber  $k$  and spin index  $\sigma$  in  $\alpha$  electrode.  $\alpha$  indicates the top or bottom metal electrode.  $\varepsilon_0(i)$  represents the  $i$ th energy level of eigenstates of the molecule.  $a_{i,\sigma}^+$  and  $a_{i,\sigma}$  are creation and annihilation operators for electrons of spin index  $\sigma$  in the  $i$ th energy level of the molecule.  $V_{\alpha}$  is the transfer matrix between the molecule and the  $\alpha$  electrode. In this calculation, we assume the molecule has two energy levels of  $\varepsilon_0(1)=0.95$  eV and  $\varepsilon_0(2)=1.95$  eV, which are estimated from Fermi levels  $E_F$  of the metal electrode, imagining that QC devices consist of the Ni electrodes and the sandwiched molecule of a P3HT:PCBM organic molecule, as shown in Fig. 13(a) (Eastman, 1970; Thompson et al., 2008).  $E_F$  is assumed to be 9.071 eV for Ni electrodes (Wang et al., 1977). Considering  $H_t$  as a perturbation, we can derive a formula for the  $I$ - $V$  characteristics from the top to the bottom electrode using the many-body perturbation technique. As a result, the current flowing from the top to the bottom electrode can be expressed by

$$I = \frac{2e^2}{h} \int_{E_F}^{E_F+eV} d\varepsilon \sum_i \left( \frac{4\Gamma_T(\varepsilon)\Gamma_B(\varepsilon)}{(\varepsilon-\varepsilon_0(i))^2 + (\Gamma_T(\varepsilon) + \Gamma_B(\varepsilon))^2} \right) [f(\varepsilon - eV - E_F) - f(\varepsilon - E_F)], \quad (14)$$

where  $e$  is the elementary charge and  $f(\varepsilon)$  is the Fermi-Dirac distribution function.  $\Gamma_{T(B)}(\varepsilon)$  is the coupling strength between the top (bottom) Ni electrode and the P3HT:PCBM organic molecule, which is given by

$$\Gamma_{T(B)}(\varepsilon) = \pi D_{T(B)}(\varepsilon) |V_{T(B)}|^2, \quad (15)$$

where  $D_{T(B)}(\varepsilon)$  is a density of states of electrons for the top (bottom) Ni electrode and  $V_{T(B)}$  is the coupling constant between the top (bottom) Ni electrode and the P3HT:PCBM organic molecule. Fig. 13(b) shows the calculated  $I$ - $V$  characteristics for Ni/P3HT:PCBM/Ni QC devices under the strong coupling limit.  $V_{T(B)}$  is assumed to be 10.0 meV, corresponding to  $\Gamma_{T(B)}$  of 3927 meV. We have obtained the ohmic  $I$ - $V$  characteristics with a resistance of 6.7 k $\Omega$ . Fig. 14 shows the experimental results of  $I$ - $V$  characteristics for Ni/P3HT:PCBM/Ni QC devices at room temperature. The inset represents the experimental setup. The Ni thickness is 16 nm. Therefore, the junction area is 16 $\times$ 16 nm<sup>2</sup>. We have obtained ohmic characteristics with a junction resistance of 32  $\Omega$ . Here, we compare this experimental value with the

calculation result. The calculation result has demonstrated that the resistance is  $6.7 \text{ k}\Omega$ , where the junction area is  $1 \times 1 \text{ nm}^2$ , which is expected as a size of one P3HT:PCBM organic molecule. The number of the conductance channel is four, taking into consideration the spin degeneracy. On the other hand, in experiments, the junction area of P3HT:PCBM organic molecules is  $16 \times 16 \text{ nm}^2$ , which corresponds to  $1024 (=4 \times 16 \times 16)$  conductance channels.

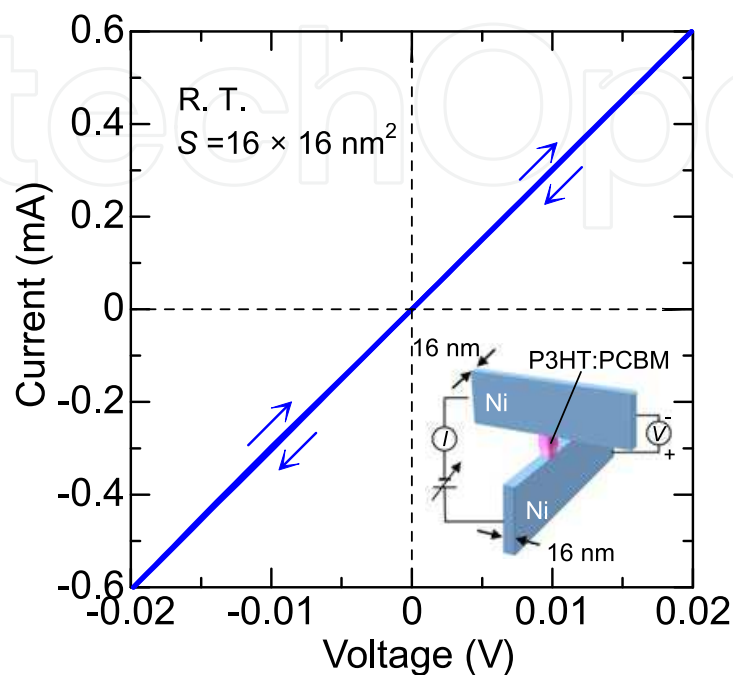


Fig. 14. Experimental results of  $I$ - $V$  characteristics for Ni/P3HT:PCBM/Ni QC devices with a junction area of  $16 \times 16 \text{ nm}^2$  at room temperature. The inset represents the experimental setup.

Therefore, the junction resistance in a size of  $16 \times 16 \text{ nm}^2$  is calculated to be  $26 \Omega (=6.7 \text{ k}\Omega / 16 / 16)$ , which is in good agreement with the experimental value of  $32 \Omega$ . This result indicates that electrons in nanoscale junctions can transport through the molecules in the ballistic regime without any scattering. This also demonstrates that our method to fabricate nanoscale junctions utilizing thin-film edges can be a useful tool for the creation of nanoscale molecular devices.

#### 4.3.3 Possibility of Ni/P3HT:PCBM/Ni QC devices for switching devices

Finally, we have discussed the possibility of Ni/P3HT:PCBM/Ni QC devices for switching devices with high on-off ratios. Fig. 15 shows the calculated  $I$ - $V$  characteristics for Ni/P3HT:PCBM/Ni QC devices under the weak coupling condition.  $V_{T(B)}$  is assumed to be  $0.2 \text{ meV}$ , corresponding to  $\Gamma_{T(B)}$  of  $1.57 \text{ meV}$ . From Fig. 15, the calculated result shows the sharp steps at the positions of the energy level of the P3HT:PCBM organic molecule. The off-state current  $I_0$  is  $3.8 \text{ pA}$  at the voltage  $V_0$  of  $0.03 \text{ V}$ , and the on-state current  $I_1$  is  $0.57 \mu\text{A}$  at the voltage  $V_1$  of  $1.03 \text{ V}$ . As we estimate the switching on-off ratio, the  $I_1/I_0$  ratio is found to be in excess of  $100000:1$ . Here, it should be noted that it is essentially important that the junction area is as small as nanometer scale in order to obtain such a high on-off ratio. When the junction area is as large as micrometer scale, the number of molecules sandwiched between the electrodes is large, so the energy level can be broadened. In contrast, when the

junction area is as small as nanometer scale, the number of molecule is small, so the energy level can be discrete. This discrete energy level leads to the sharp steps in the  $I$ - $V$  characteristics, which can produce such a high switching ratio. Thus, Ni/P3HT:PCBM/Ni QC devices utilizing thin-film edges can be expected to have potential application in switching devices with high on-off ratios.

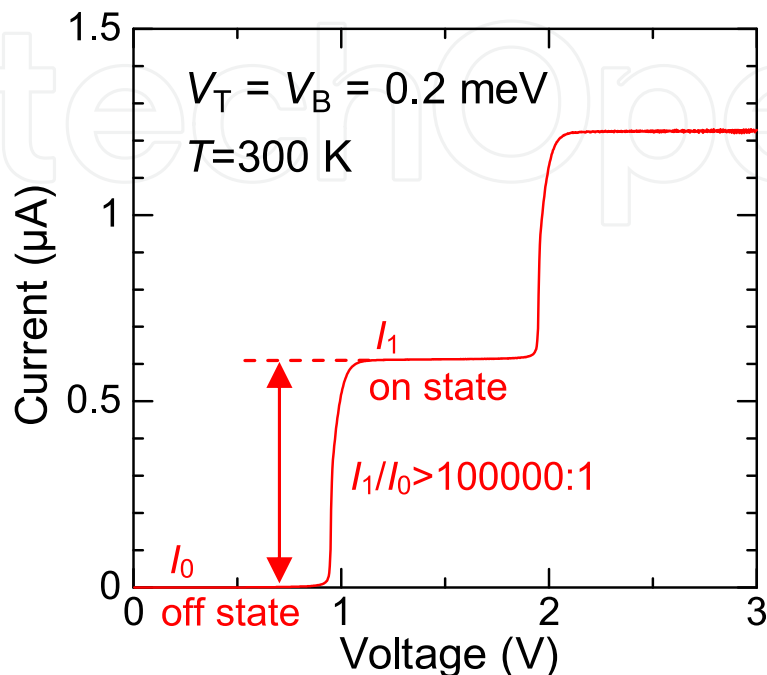


Fig. 15. Calculated  $I$ - $V$  characteristics for Ni/P3HT:PCBM/Ni QC devices under the weak coupling condition.

## 5. Conclusions

In this chapter, we have introduced structural and electrical properties of Ni/PEN films used as electrodes in QC devices and  $I$ - $V$  characteristics for three types of QC devices. The three types of QC devices are as follows: (i) Ni/Ni QC devices (17 nm linewidth,  $17 \times 17$  nm<sup>2</sup> junction area), in which two Ni thin films are directly contacted with their edges crossed, (ii) Ni/NiO/Ni QC devices (24 nm linewidth,  $24 \times 24$  nm<sup>2</sup> junction area), in which NiO thin insulators are sandwiched between two Ni thin-film edges and (iii) Ni/P3HT:PCBM/Ni QC devices (16 nm linewidth,  $16 \times 16$  nm<sup>2</sup> junction area), in which P3HT:PCBM organic molecules are sandwiched between two Ni thin-film edges. In our study, we have successfully fabricated various types of QC devices with nano-linewidth and nano-junctions, which have been obtained without the use of electron-beam or optical lithography. Our method will open up new opportunities for the creation of nanoscale patterns and can also be expected as novel technique beyond conventional lithography. Furthermore, we have presented the calculation results of the electronic transport in Ni/organic-molecule/Ni QC devices and discussed their possibility for switching devices. According to our calculation, a high switching ratio in excess of 100000:1 can be obtained under weak coupling condition. These results indicate that QC devices fabricated using thin-film edges can be expected to have potential application in next-generation switching devices with ultrahigh on-off ratios.

## 6. Acknowledgment

This research has been partially supported by the Management Expenses Grants for National Universities Corporations and a Grant-in-Aid for Young Scientists from The Ministry of Education, Culture, Sports, Science and Technology (MEXT), Precursory Research for Embryonic Science and Technology program from Japan Science and Technology Agency (JST) and a Grant-in-Aid for Scientific Research from Japan Society for the Promotion of Science (JSPS). The authors would like to express their sincere appreciation to Dr. M. Hirasaka of Teijin Ltd. and Research Manager K. Kubo of Teijin DuPont Films Japan Ltd. for supplying PEN organic films, Prof. Y. Hirotsu, Assoc. Prof. M. Ishimaru and Assist. Prof. A. Hirata at Osaka University for investigating cross-sectional TEM images and ED patterns, Y. Inoue of Meiwafoysis Co., Ltd. for examining the fabrication of NiO insulators and Prof. M. Yamamoto, Assist. Prof. K. Matsuda, A. Ono, N. Basheer, N. Kawaguchi, S. White, H. Sato and M. Takei at Hokkaido University for their cooperation and helpful discussions.

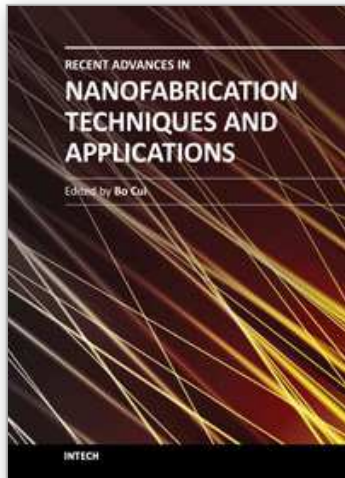
## 7. References

- Balzani, V., Credi, A., Mattersteig, G., Matthews, O. A., Raymo, F. M., Stoddart, J. F., Venturi, M.; White, A. J. P. & Williams, D. J. J. (2000). *Org. Chem.* 65: 1924.
- Cai, T., Han, H., Yu, Y., Gao, T., Du, J. & Hao, L. (2009). *Physica B* 404: 89.
- Chen, J., Reed, M. A., Rawlett, A. M. & Tour, J. M. (1999). *Science* 286: 1550.
- Chen, Y., Ohlberg, D. A. A., Li, X., Stewart, D. R., Williams, R. S., Jeppesen, J. O., Nielsen, K. A., Stoddard, J. F., Olynick, D. L. & Anderson, R. (2003). *Appl. Phys. Lett.* 82: 1610.
- Chevrier, J., Lethanh, V., Buys, R. & Derrien, J. (1991). *Europhys. Lett.* 16: 737.
- Doudin, B., Redmond, G., Gilbert, S. E. & Ansermet, J. -Ph. (1997). *Phys. Rev. Lett.* 79: 933.
- Dürr, A. C., Schreiber, F., Kelsch, M., Carstanjen, H. D. & Dosch, H. (2002). *Adv. Mater.* 14: 961.
- Eastman, D. E. (1970). *Phys. Rev. B* 2: 1.
- Elp, J., Eskes, H., Kuiper, P. & Sawatzky, G. A. (1992). *Phys. Rev. B* 45: 1612.
- Finders, J., Dusa, M., Vleeming, B., Megens, H., Hepp, B., Maenhoudt, M., Cheng, S. & Vandeweyer, T. (2008). *Proc. SPIE* 6924: 692408.
- Finkler, A., Segev, Y., Myasoedov, Y., Rappaport, M. L., Ne'eman, L., Vasyukov, D., Zeldov, E., Huber, M. E., Martin, J. & Yacoby, A. (2010). *Nano Lett.* 10: 1046.
- Fujikawa, S., Takaki, R. & Kunitake, T. (2006). *Langmuir* 22: 9057.
- Fumeaux, C., Herrmann, W., Rothuizen, H., Natale, P. D. & Kneubuehl, F. K. (1996). *Appl. Phys. B* 63: 135.
- Green, J. E., Choi, J. W., Boukai, A., Bunimovich, Y., Johnston-Halperin, E., Delonno, E., Luo, Y., Sheriff, B. A., Xu, K., Shin, Y. S., Tseng, H.-R., Stoddart, J. F. & Heath, J. R. (2007). *Nature* 445: 414.
- Hayakawa, J., Ikeda, S., Miura, K., Yarnanouchi, M., Lee, Y. M., Sasaki, R., Ichimura, M., Ito, K., Kawahara, T., Takemura, R., Meguro, T., Matsukura, F., Takahashi, H., Matsuoka, H. & Ohno, H. (2008). *IEEE Trans. Mag.* 44: 1962.
- Hirose, Y., Kahn, A., Aristov, V. & Soukiassian, P. (1996). *Appl. Phys. Lett.* 68: 217.
- Hobbs, P. C. D., Laibowitz, R. B. & Libsch, F. R. (2005). *Appl. Opt.* 44: 6813.

- Huber, M. E., Koshnick, N. C., Bluhm, H., Archuleta, L. J., Azua, T., Bjornsson, P. G., Gardner, B. W., Halloran, S. T., Lucero, E. A. & Moler, K. A. (2008). *Rev. Sci. Instrum.* 79: 053704.
- Ishibashi, A. (2003). Jpn. Pat. 3974551.
- Ishibashi, A. (2004). *Proceedings of International Symposium on Nano Science and Technology*, pp. 44-45, Tainan, Taiwan, November 20-21, 2004.
- Ishibashi, A., Kaiju, H., Yamagata, Y. & Kawaguchi, N. (2005). *Electron. Lett.* 41: 735.
- Ito, E., Oji, H., Furuta, M., Ishii, H., Oichi, K., Ouchi, Y. & Seki, K. (1999). *Synthetic Metals* 101: 654.
- Kaiju, H., Kawaguchi, N. & Ishibashi, A. (2005). *Rev. Sci. Instrum.* 76: 085111.
- Kaiju, H., Ono, A., Kawaguchi, N. & Ishibashi, A. (2008). *Jpn. J. Appl. Phys.* 47: 244.
- Kaiju, H., Ono, A., Kawaguchi, N. & Ishibashi, A. (2008). *J. Appl. Phys.* 103: 07B523.
- Kaiju, H., Ono, A., Kawaguchi, N., Kondo, K., Ishibashi, A., Won, J. H., Hirata, A., Ishimaru, M. & Hirotsu, Y. (2009). *Appl. Surf. Sci.* 255: 3706.
- Kaiju, H., Kondo, K., Ono, A., Kawaguchi, N., Won, J. H., Hirata, A., Ishimaru, M., Hirotsu, Y. & Ishibashi, A. (2010). *Nanotechnology* 21: 015301.
- Kaiju, H., Kondo, K., Basheer, N., Kawaguchi, N., White, S., Hirata, A., Ishimaru, M., Hirotsu, Y. & Ishibashi, A. (2010). *Mater. Res. Soc. Symp. Proc.* 1252: J0208.
- Kaiju, H., Basheer, N., Kondo, K. & Ishibashi, A. (2010). *IEEE Trans. Magn.* 46: 1356.
- Kaiju, H., Kondo, K. & Ishibashi, A. (2010). *Jpn. J. Appl. Phys.* 49: 105203.
- Kale, B. M. (1985). *Opt. Eng.* 24: 267.
- Kardar, M., Parisi, G. & Zhang, Y. -C. (1986). *Phys. Rev. Lett.* 56: 889.
- Kirtley, J. R. (2009). *Supercond. Sci. Technol.* 22: 064008.
- Kondo, K. & Ishibashi, A. (2006). *Jpn. J. Appl. Phys.* 45: 9137.
- Kondo, K., Kaiju, H. & Ishibashi, A. (2008). *Mater. Res. Soc. Symp. Proc.* 1067: B0301.
- Kondo, K., Kaiju, H. & Ishibashi, A. (2009). *J. Appl. Phys.* 105: 07D522.
- Kondo, K., Kaiju, H. & Ishibashi, A. (2010). *Mater. Res. Soc. Symp. Proc.* 1198: E0701.
- Kondo, K. (2010). *J. Appl. Phys.* 107: 09C709.
- Kuiper, P., Kruizinga, G., Ghijsen, J., Sawatzky, G. A. & Verweij, H. (1989). *Phys. Rev. Lett.* 62: 221.
- Kwon, S., Yan, X., Contreras, A. M., Liddle, J. A., Somorjai, G. A. & Bokor, J. (2005). *Nano Lett.* 5: 2557.
- Lau, C. N., Stewart, D. R., Williams, R. S. & Bockrath, M. (2004). *Nano Lett.* 4: 569.
- Mayadas, A. F. & Shatzkes, M. (1970). *Phys. Rev. B* 1: 1382.
- Melosh, N. A., Boukai, A., Diana, F., Gerardot, B., Badolato, A., Petroff, P. M. & Heath, J. R. (2003). *Science* 300: 112.
- Mendes, P. M., Flood, A. H. & Stoddart, J. F. (2005). *Appl. Phys. A* 80: 1197.
- Miyazaki, T. & Tezuka, N. (1995). *J. Magn. Magn. Mater.* 139: L231.
- Moodera, J. S., Kinder, L. R., Wong, T. M. & Meservey, R. (1995). *Phys. Rev. Lett.* 74: 3273.
- Nacereddine, C., Layadi, A., Guittoum, A., Cherif, S. -M., Chauveau, T., Billet, D., Youssef, J. B., Bourzami, A. & Bourahli, M. -H. (2007). *Mater. Sci. Eng. B* 136: 197.
- Naulleau, P. P., Anderson, C. N., Chiu, J., Denham, P., George, S., Goldberg, K. A., Goldstein, M., Hoef, B., Hudyma, R., Jones, G., Koh, C., Fontaine, B. L., Ma, A., Montgomery, W., Niakoula, D., Park, J.-o., Wallow, T. & Wurm, S. (2009). *Microelectron. Eng.* 86: 448.

- Nawate, M., Shinohara, K., Honda, S. & Tanaka, H. (2004). *Trans. Mater. Res. Soc. Jpn.* 29: 1599.
- Ohkawa, K., Nakano, T. & Baba, S. (2002). *J. Vac. Soc. Jpn.* 45: 134.
- Ono, K., Shimada, H. & Ootuka, Y. (1997). *J. Phys. Soc. Jpn.* 66: 1261.
- Palasantzas, G. & Krim, J. (1994). *Phys. Rev. Lett.* 73: 3564.
- Parkin, S. S., Kaiser, C., Panchula, A., Rice, P. M., Hughes, B., Samant, M. & Yang, S.-H. (2004). *Nat. Mater.* 3: 862.
- Pease, A. R., Jeppesen, J. O., Stoddart, J. F., Luo, Y., Collier, C. P. & Heath, J. R. (2001). *Acc. Chem. Res.* 36: 433.
- Rahaman, M. D., Kaiju, H., Kawaguchi, N. & Ishibashi, A. (2008). *Jpn. J. Appl. Phys.* 47: 5712.
- Reed, M. A., Chen, J., Rawlett, A. M., Price, D. W. & Tour, J. M. (2001). *Appl. Phys. Lett.* 78: 3735.
- Rugar, D., Budakian, R., Mamin, H. J. & Chui, B. W. (2004). *Nature* 430: 329.
- Sanchez, A., Davis, C. F., Liu, K. C. & Javan, A. (1978). *J. Appl. Phys.* 49: 5270.
- Sawatzky, G. A. & Allen, J. W. (1984). *Phys. Rev. Lett.* 53: 2339.
- Sewell, H., Chen, A., Finders, J. & Dusa, M. (2009). *Jpn. J. Appl. Phys.* 48: 06FA01.
- Tarlov, M. J. (1992). *Langmuir* 8: 80.
- Thompson, B. C. & Fréchet, J. M. (2008). *J. Angew. Chem. Int. Ed.* 47: 58.
- Thompson, C., Palasantzas, G., Feng, Y. P., Sinha, S. K. & Krim, J. (1994). *Phys. Rev. B* 49: 4902.
- Tong, W. M., Williams, R. S., Yanase, A., Segawa, Y. & Anderson, M. S. (1994). *Phys. Rev. Lett.* 72: 3374.
- Troeman, A. G. P., Derking, H., Borger, B., Pleikies, J., Veldhuis, D. & Hilgenkamp, H. (2007). *Nano Lett.* 7: 2152.
- Vries, J. W. C. (1987). *Thin Solid Films* 150: 209.
- Wang, C. S. & Callaway, J. (1977). *Phys. Rev. B* 15: 298.
- Wilke, I., Oppliger, Y., Herrmann, W. & Kneubuehl, F. K. (1994). *Appl. Phys. A* 58: 329.
- Wu, W., Jung, G.-Y., Olynick, D. L., Straznicki, J., Li, Z., Li, X., Ohlberg, D. A. A., Chen, Y., Wang, S. -Y., Liddle, J. A., Tong, W. M. & Williams, R. S. (2005). *Appl. Phys. A* 80: 1173.
- Yuasa, S., Nagahama, T., Fukushima, A., Suzuki, Y. & Ando, K. (2004). *Nat. Mater.* 3: 868.

IntechOpen



## **Recent Advances in Nanofabrication Techniques and Applications**

Edited by Prof. Bo Cui

ISBN 978-953-307-602-7

Hard cover, 614 pages

**Publisher** InTech

**Published online** 02, December, 2011

**Published in print edition** December, 2011

Nanotechnology has experienced a rapid growth in the past decade, largely owing to the rapid advances in nanofabrication techniques employed to fabricate nano-devices. Nanofabrication can be divided into two categories: "bottom up" approach using chemical synthesis or self assembly, and "top down" approach using nanolithography, thin film deposition and etching techniques. Both topics are covered, though with a focus on the second category. This book contains twenty nine chapters and aims to provide the fundamentals and recent advances of nanofabrication techniques, as well as its device applications. Most chapters focus on in-depth studies of a particular research field, and are thus targeted for researchers, though some chapters focus on the basics of lithographic techniques accessible for upper year undergraduate students. Divided into five parts, this book covers electron beam, focused ion beam, nanoimprint, deep and extreme UV, X-ray, scanning probe, interference, two-photon, and nanosphere lithography.

### **How to reference**

In order to correctly reference this scholarly work, feel free to copy and paste the following:

Hideo Kaiju, Kenji Kondo and Akira Ishibashi (2011). Lithography-Free Nanostructure Fabrication Techniques Utilizing Thin-Film Edges, Recent Advances in Nanofabrication Techniques and Applications, Prof. Bo Cui (Ed.), ISBN: 978-953-307-602-7, InTech, Available from: <http://www.intechopen.com/books/recent-advances-in-nanofabrication-techniques-and-applications/lithography-free-nanostructure-fabrication-techniques-utilizing-thin-film-edges>

**INTECH**  
open science | open minds

### **InTech Europe**

University Campus STeP Ri  
Slavka Krautzeka 83/A  
51000 Rijeka, Croatia  
Phone: +385 (51) 770 447  
Fax: +385 (51) 686 166  
[www.intechopen.com](http://www.intechopen.com)

### **InTech China**

Unit 405, Office Block, Hotel Equatorial Shanghai  
No.65, Yan An Road (West), Shanghai, 200040, China  
中国上海市延安西路65号上海国际贵都大饭店办公楼405单元  
Phone: +86-21-62489820  
Fax: +86-21-62489821



© 2011 The Author(s). Licensee IntechOpen. This is an open access article distributed under the terms of the [Creative Commons Attribution 3.0 License](#), which permits unrestricted use, distribution, and reproduction in any medium, provided the original work is properly cited.

IntechOpen

IntechOpen